THE JOURNAL OF PHYSICAL CHEMISTRY C
A JOURNAL OF THE AMERICAN CHEMICAL SOCIETY

pubs.acs.org/JPCC

Article

Low Energy Electron- and Ion-Induced Surface Reactions of $Fe(CO)_5$ Thin Films

Published as part of The Journal of Physical Chemistry virtual special issue "125 Years of The Journal of Physical Chemistry".

Elif Bilgilisoy, Rachel M. Thorman, Michael S. Barclay, Hubertus Marbach, and D. Howard Fairbrother*

Cite This: *J. Phys. Chem. C* 2021, 125, 17749–17760

Read Online

ACCESS | Metrics & More | Article Recommendations | Supporting Information

ABSTRACT: Using *in situ* X-ray photoelectron spectroscopy (XPS), the effects of low energy (500 eV) electrons and low energy (1200 eV) Ar^+ ions on thin films of $Fe(CO)_5$, a prototypical organometallic precursor, have been investigated. These studies were motivated by the important role that these surface reactions play in the charged-particle-induced deposition of nanostructures. XPS data from the C(1s) and O(1s) regions were used to construct kinetic models to describe the effects of electron and ion irradiation, both of which occurred through a sequence of two sequential surface reactions, although the details of each step differ. During electron irradiation, precursor molecules initially decompose as a result of electronic excitation, resulting in desorption of approximately 50% of the CO ligands and partial decarbonylation within the $Fe(CO)_5$ film. In the second step, the partially decarbonylated intermediates undergo a much slower electron-stimulated CO decomposition process to produce iron oxides encased in a graphitic film. $Fe_2(CO)_9$ and $Fe_3(CO)_{12}$ reacted similarly to $Fe(CO)_5$, but the initial rate of decomposition was an order of magnitude higher. During Ar^+ bombardment, $Fe(CO)_5$ molecules decompose as a consequence of energy transfer from the incident ions, causing complete fragmentation of the precursor and desorption of ≈80% of the CO molecules. The remaining 20% undergo C≡O bond cleavage, forming adsorbed carbon and volatile oxygen species. In the second step of the reaction, the residual iron and carbon atoms are subject to Ar^+ ion sputtering. The implications of these reactions for focused ion beam-induced deposition (FIBID) and focused electron beam-induced deposition (FEBID) from $Fe(CO)_5$ are also discussed.

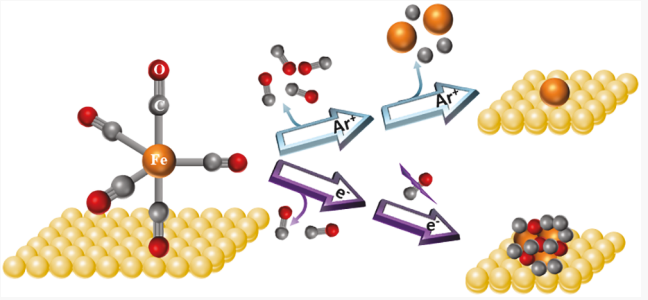

INTRODUCTION

Focused electron-beam-induced deposition (FEBID) and focused ion-beam-induced deposition (FIBID) are powerful lithographic techniques for the fabrication of nanostructures.[1−3] Both techniques utilize tightly focused charged particle (electron or ion) beams to directly write three-dimensional nanostructures onto surfaces of any dimensionality (i.e., planar or nonplanar). In FEBID and FIBID, an organometallic precursor is typically introduced into a high vacuum (HV) chamber where interactions between the charged particle beam and the transiently adsorbed precursor decompose the molecule. Involatile fragments form a deposit, while volatile fragments desorb. Ideally, the deposit contains only metal atoms, but unwanted organic contaminants are invariably present. Both FEBID and FIBID have been used to produce a variety of three-dimensional ferromagnetic nanostructures composed of iron and cobalt from organometallic precursors such as $Fe(CO)_5$, $Co_2(CO)_8$, and $Co(CO)_3NO$.[1,2]

In FEBID, fabrication of iron nanostructures has been performed using $Fe(CO)_5$,[1,2,4,5] $Fe_3(CO)_{12}$,[6] $Fe_2(CO)_9$,[7] and $Fe(C_5H_5)_2$ (ferrocene).[8] Of these precursors, $Fe(CO)_5$ and $Fe_2(CO)_9$ have produced deposits with the highest iron purities (>80 at. % Fe),[4,5,7] with carbon and oxygen as contaminants; $Fe(CO)_5$ is by far the most popular iron-containing precursor used in FEBID.[1,2] By varying deposition parameters, Gavagnin et al. were able to produce deposits with an iron-to-oxygen ratio of 11.8:1; assuming similar concentrations of carbon to oxygen, the purity of these deposits was about 85 at. % Fe.[4] To achieve pure iron deposition from $Fe(CO)_5$, Lukasczyk et al. made deposits with purities of >95 at. % Fe in UHV.[5] To our knowledge, the only iron deposits made with FIBID were micron-scale lines printed with a 50 kV Ga^+ focused ion beam using $Fe(CO)_5$ as a precursor, achieving

Received: June 30, 2021
Revised: July 28, 2021
Published: August 7, 2021

https://doi.org/10.1021/acs.jpcc.1c05826
J. Phys. Chem. C 2021, 125, 17749−17760

a maximum purity of 85 at. % Fe as measured by Auger electron spectroscopy.[9]

For FEBID and FIBID to continue to develop as nanofabrication tools, it is necessary to better understand the electron- and ion-induced reactions that accompany deposition. In FEBID, low energy (<100 eV) secondary electrons generated by interactions between the high energy primary electron beam and the substrate are significant contributors to reactions that occur during deposition.[2,10] In this regard, low energy electron interactions with gas phase $Fe(CO)_5$ molecules have been well-studied, including studies of isolated $Fe(CO)_5$ molecules,[11,12] clusters containing $Fe(CO)_5$,[13,14] and mixed $Fe(CO)_5/H_2O$ clusters.[15] The advantage of these studies is that electron-energy dependent reaction mechanisms can be identified, although only the initial electron-molecule interactions can be probed and the absence of a substrate means that conditions are quite different to those pertinent to FEBID. The most intensively studied low energy electron-induced reactions are dissociative electron attachment (DEA) and dissociative ionization (DI).[10] In DEA, a low energy electron (typically <5 eV) attaches to a precursor, forming a transient negative ion which then dissociates into an anionic fragment and one or more neutral fragments. For higher energy secondary electrons (typically >10 eV) DI becomes effective, where electron impact ionizes a precursor molecule, forming a cation which then dissociates into a cationic fragment and one or more neutral fragments.

Early DEA findings by Compton et al. using low energy electrons (<10 eV) identified $Fe(CO)_4^-$ as the principal fragment, with a maximum cross-section at incident energies of approximately 0.5 eV;[16] $Fe(CO)_3^-$ and $Fe(CO)_2^-$ were also observed for incident energies between 3−6 eV, but at much lower intensities compared to $Fe(CO)_4^-$. This finding was corroborated by a more recent DEA study of $Fe(CO)_5$ molecules by Allan et al.[11] The DI of $Fe(CO)_5$ has also been studied by a number of groups.[12,14,16,17] The results of Lacko et al.[12] are illustrative with much more $Fe(CO)_5$ fragmentation observed as compared to DEA, with a predominance of Fe−CO dissociation and the formation of $Fe(CO)_x^+$ daughter ions; at an incident energy of 70 eV the fragment with the highest intensity was $Fe(CO)^+$. Low energy electron interaction with gas phase clusters of $Fe(CO)_5$ have also be conducted, representing a step closer to FEBID by including intermolecular interactions. DEA processes involving pure $Fe(CO)_5$ clusters, and $Fe(CO)_5$/Ar clusters[13,18] again identified $Fe(CO)_4^-$ as the primary product, although its intensity was lower than observed for the isolated gas phase studies, suggesting that DEA is suppressed by intermolecular interactions.[13] In contrast to the isolated gas phase studies, ions containing two and three iron atoms were identified. The synthesis of these more complex heteronuclear anions was attributed to self-scavenging,[18] where anions attach to monomer units. Lengyel et al. investigated the DI fragmentation of pure $Fe(CO)_5$ clusters, and $Fe(CO)_5$/Ar clusters.[14] Both clusters yielded less fragmentation than in the isolated gas phase, with the formation of the dominant cationic fragmentation, $Fe(CO)_2^+$, being ascribed to the electron impact ionization of argon followed by an electron−hole transfer to $Fe(CO)_5$ clusters.

A number of UHV surface science studies have investigated electron interactions with adsorbed $Fe(CO)_5$, a much closer approximation to the deposition conditions relevant to FEBID. In an early study, Foord et al. investigated the high energy (2.5 keV) electron-stimulated reactions of adsorbed $Fe(CO)_5$ on Si(100).[19] Multilayer $Fe(CO)_5$ was found to undergo electron stimulated desorption, while monolayer $Fe(CO)_5$ decomposed through a combination of electron stimulated CO desorption ($CO_{(ads)} \rightarrow CO_{(g)}$) and CO decomposition ($CO_{(ads)} \rightarrow C_{(ads)} + O_{(g)}$). Low energy electron-induced reactions (3−132 eV) of multilayer $Fe(CO)_5$ adsorbed on Ag(111) have been studied by Henderson et al. by using TPD, AES, and LEED.[20] Results implicated the formation of partially decrbonylated $Fe_x(CO)_y$ clusters on the surface as a result of CO desorption. These intermediate species were much less susceptible to electron-induced reactions as compared to the parent $Fe(CO)_5$ molecules, but underwent thermal decomposition at around 300 K to produce pure iron. On the Au(111)/mica surface, Hauchard et al. used grazing incidence infrared (IR) spectroscopy to examine the low energy (1−20 eV) electron-induced decomposition kinetics of $Fe(CO)_5$ thin films adsorbed on a cooled (45 K) surface.[21] A decarbonylation process was observed and a two-step sequential mechanism proposed which included the initial loss of 20−80% of CO ligands due to the formation of $Fe_x(CO)_y$ anions, and a subsequently slower process leading to complete CO loss. A more recent study by Massey et al. used MS to probe the desorption of anionic and cationic fragments from thin films of $Fe(CO)_5$ adsorbed on condensed Xe or a Pt foil and exposed to 4−33 eV electrons.[17] O^- and $Fe(CO)_x^-$ were produced at around ≥6 eV via DEA while positive ions in the form of C^+, O^+ and $Fe(CO)_x^+$ were detected at incident energies between 15−25 eV.

In contrast to the wealth of information that exists on electron interactions with $Fe(CO)_5$ there is comparatively little known about ion interactions with $Fe(CO)_5$. One notable exception is a recent study by Indrajith et al., who probed the gas phase reactions of singly and multiply charged noble gas ions (He^+/He^{2+}, Ne^+/Ne^{4+}, Ar^+/Ar^{3+}, and Kr^{3+}/Kr^{17+}) at various incident energies with isolated $Fe(CO)_5$.[22] Electronic excitation characterized the interactions between gas phase $Fe(CO)_5$ and lighter ions (i.e., He^+), leading to a low fragmentation efficiency and fragments with comparatively low kinetic energies. In contrast, collisions involving heavier ions (Ne^+, Ar^+, Kr^+), were dominated by nuclear stopping, a much greater degree of fragmentation and higher kinetic energy fragments. Interestingly, the most effective fragmentation, with over 90% CO desorption was observed for Ne^+ ions.

Previous UHV surface science studies of the low energy electron-induced decomposition of adsorbed FEBID precursors have revealed that the first step in FEBID involves low energy electron-induced dissociation of the precursor, which is invariably accompanied by the desorption of one or more ligands from the precursor.[23−28] After this initial electron-induced ligand loss step, continued electron exposure typically causes ligand decomposition, rather than dissociation and desorption from the surface.[24,29−31] Thus, any ligands remaining on the surface after the initial ligand loss step are incorporated into the deposit. Reactions that accompany FIBID, however, are far less well-understood. Secondary electrons produced by interactions between the high energy primary ion beam and the substrate may induce precursor decomposition, as in FEBID; however, due to the significantly larger mass of ions compared to electrons, energy/momentum transfer from the primary beam to the substrate and precursor molecules is also relevant in FIBID.[32,33] Thus, surface-mediated energy transfer between the primary ion beam and

https://doi.org/10.1021/acs.jpcc.1c05826
J. Phys. Chem. C 2021, 125, 17749−17760

the precursor molecules, known as the collision cascade model, may be responsible for deposition in FIBID.[3,32] Previous FIBID experiments have correlated measurements of growth rate with different parameters, such as nuclear and electronic stopping power[32,34] and secondary electron and sputtering yields,[33,35,36] in order to determine whether the secondary electron model or the collision cascade model is the valid deposition mechanism in FIBID. These studies yielded evidence for both models of deposition and, taken together, are not conclusive.

In a recent paper, we compared the low energy (<1 keV) electron- and argon ion-induced decomposition reactions of thin films of adsorbed $CpFe(CO)_2Re(CO)_5$ on a cooled gold substrate.[37] This study revealed that the electron and argon ion-induced decomposition of adsorbed $CpFe(CO)_2Re(CO)_5$ were significantly different, giving support to the collision cascade model dominating deposition in the ion-limited regime of FIBID. To explore the extent to which these differences apply to other precursors we have used *in situ* XPS in the present investigation to compare and contrast the low energy electron- (500 eV) and Ar^+ (1200−3000 eV) induced reactions with thin films of adsorbed $Fe(CO)_5$ on a cooled (143 K) Au substrate. A notable advantage of $Fe(CO)_5$ is that the C(1s) and O(1s) regions in XPS can be deconvoluted into contributions from different species (e.g., CO and C_{gr}), facilitating the development of kinetic models to describe and quantify the elementary reaction steps and reaction mechanisms.

EXPERIMENTAL METHODS

Studies were performed in a UHV chamber with a base pressure below 4×10^{-9} Torr, equipped with X-ray photoelectron spectroscopy (XPS), mass spectrometry (MS), a flood electron gun, and an ion gun.[38−40] Iron pentacarbonyl (>99.99%, Sigma-Aldrich), diiron nonacarbonyl (99%, Strem Chemicals), and triiron dodecacarbonyl (95%, Strem Chemicals) are all liquids which are sensitive to air and UV light. Each iron carbonyl was therefore loaded into a glass vessel in a glovebox under N_2 atmosphere, attached to a UHV compatible leak valve, and wrapped with aluminum foil. The leak valve itself was then attached to the UHV chamber before being subject to several freeze pump thaw cycles. Iron carbonyls were introduced into the UHV chamber via the leak valve and dosed onto a gold substrate cooled to 143 ± 5 K to create a thin film. Film thicknesses were measured by monitoring the attenuation of the Au substrate peaks using XPS.[38−40]

X-ray photoelectron spectroscopy was performed using a PHI 5400 XPS with a Mg Kα ($h\nu$ = 1254 eV) anode. Spectra were calibrated using the Au($4f_{7/2}$) peak associated with the substrate (BE = 84.0 eV)[41] and processed using CasaXPS, a commercially available software. The electron source used during the electron irradiation studies was a Specs FG 15/40. The ion gun used in argon ion irradiation studies was a PerkinElmer PHI model 04−303 differentially pumped ion gun.

During both the electron and argon ion irradiation studies, the substrate was biased by +20 V to ensure that all secondary electrons generated by electron or argon ion irradiation remained on the substrate, and the respective beams were defocused to ensure that the entire 1 cm^2 surface was exposed to ions or electrons. Previous studies have established that the flood gun produces a uniform flux of electron across the surface.[42] In the electron irradiation studies, a primary electron beam energy of +480 eV was used, producing an incident electron energy of +500 eV, and the target current was maintained at 30 μA. The electron beam was oriented along the surface normal of the sample. Electron irradiation is reported in terms of electron dose (e^-/cm^2) and current density (mC/cm^2). In the argon irradiation studies, primary beam energies of 1200 and 3000 eV were used, producing an incident argon ion energy of 1180 and 2980 eV. The argon ion beam was oriented at approximately 45° from the surface normal. Based on separate deposition experiments the ion gun was determined to produce a Gaussian distribution of ion intensity on the surface. Argon ion irradiation is reported in terms of ion dose (mC/cm^2).

RESULTS AND DISCUSSION

Electron-Induced Reactions. Figure 1 shows how the C(1s), O(1s), and Fe(2p) XPS regions of adsorbed $Fe(CO)_5$

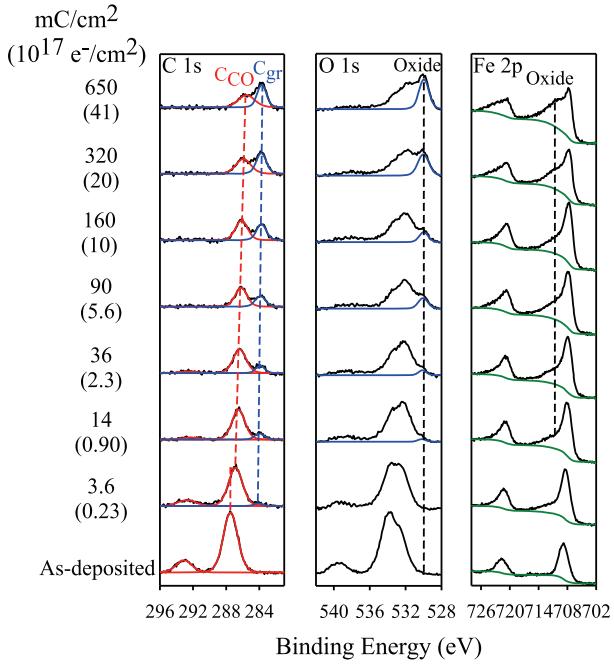

Figure 1. Evolution of the C(1s), O(1s), and Fe(2p) XPS regions of ≈1.8−2.6 nm thin films of $Fe(CO)_5$ upon irradiation with 500 eV electrons. The bottom spectra represent the as-deposited, unirradiated film. Speciation is shown in the C(1s) region, where the red line represents the C(1s) peak associated with the precursor carbonyl ligands while the blue lines represent the C(1s) peak associated with the graphitic carbon species in the deposit. The dashed red and blue lines in this region show the change in binding energy of these peaks during electron irradiation. The black dashed lines in the O(1s) and Fe(2p) regions indicate oxide growth. The green curves in the Fe(2p) region show the background. Electron dose is shown on the left-hand side in units of mC/cm^2 and, in parentheses, 10^{15} e^-/cm^2.

thin films (1.8−2.6 nm) respond to irradiation with 500 eV electrons. Control studies on the effect of X-ray irradiation (Figure S1) demonstrate that adsorbed $Fe(CO)_5$ thin films were relatively unaltered by X-rays over the irradiation times required to acquire XPS spectra; thus changes in the C(1s), O(1s), and Fe(2p) XPS regions can all be ascribed to the effects of electron irradiation. The C(1s) region associated with the as-deposited $Fe(CO)_5$ precursor is characterized by 2 peaks, shown as solid red curves: a high intensity peak at 287.5

https://doi.org/10.1021/acs.jpcc.1c05826
J. Phys. Chem. C 2021, 125, 17749−17760

eV and a lower intensity, higher binding energy peak at 293.1 eV. The high intensity peak at 287.5 eV is assigned to photoelectrons from the C(1s) orbital of the *CO* ligands, while the lower intensity peak at 293.1 eV is a $\pi-\pi^*$ shakeup peak typically observed for metal carbonyls.[43] Before electron irradiation, the O(1s) region is characterized by three peaks. The two lower binding energy peaks overlap significantly, forming a larger, asymmetrical peak centered at approximately 533.6 eV and are assigned to photoelectrons from the O(1s) orbital of the *CO* ligands;[44] the asymmetry is similar to that previously observed for CO adsorbed on Fe(100).[45] The third, higher binding energy peak at 539.6 eV is the *CO* $\pi-\pi^*$ shakeup peak.[43] The Fe(2p) region is initially characterized by two asymmetric peaks at approximately 708.8 and 721.7 eV, corresponding to $Fe(2p_{3/2})$ and $Fe(2p_{1/2})$ transitions, respectively.[44,46] The C(1s) and O(1s) regions have had their respective backgrounds removed, while in the Fe(2p) region the background is shown as a green curve.

Upon irradiation with 500 eV electrons, both peaks in the C(1s) region decrease in intensity; after an electron dose of 3.6 mC/cm^2, the *CO* peak at 287.5 eV has shifted to a lower binding energy of 286.8 eV and a new lower binding energy peak appears at approximately 284.1 eV, shown in Figure 1 as a blue curve. The binding energy of this peak suggests that it is associated with graphitic carbon species.[24] Continued electron irradiation causes the peaks associated with the CO ligands to continue to decrease in intensity and shift to lower binding energy, while the lower binding energy graphitic carbon peak increases in intensity.

Electron irradiation also causes the main asymmetric O(1s) peak associated with the *CO* oxygen species to decrease in intensity and shift to slightly lower binding energy. At the same time, a lower binding energy peak grows in at approximately 530.2 eV, ascribed to an iron oxide.[47] This peak, shown in Figure 1 as a blue solid curve with a black dashed line, becomes discernible after an electron dose of about 14 mC/cm^2; similar to the graphitic carbon species in the C(1s) region. Continued electron irradiation causes the oxide peak to increase in intensity, while the *CO* species decrease in intensity and shift to lower binding energy. After an effective electron dose of 650 mC/cm^2, the O(1s) region is characterized by a clearly resolved oxide peak at 529.9 eV,[47] as well as features at higher binding energies associated with residual CO species.

In the Fe(2p) region, electron irradiation causes the Fe(2p) peaks to shift and broaden to lower binding energies. As the lower binding energy oxide peak grows in the O(1s) region, a higher binding energy shoulder also becomes apparent in the Fe(2p) region. This feature continues to increase in intensity with larger electron doses and is clearly resolved for electron doses in excess of 320 mC/cm^2. The Fe(2p) region is characterized by two peaks at 707.8 and 720.7 eV after an electron dose of 650 mC/cm^2, along with a higher binding energy shoulder with a peak at approximately 710.3 eV, the latter indicative of an iron oxide.[47,48] In contrast to carbon and oxygen, no iron atoms desorb during electron irradiation.

Figure 2a shows the decrease in the fractional coverage of carbon and oxygen atoms as a function of electron dose in mC/cm^2 (bottom axis) and e$^-$/cm^2 (top axis). Both elements follow a similar kinetic dependence, with a rapid decrease in coverage to approximately half of their initial value during the initial 20 mC/cm^2 electron dose but remaining constant thereafter. The similar rate and extent of carbon and oxygen loss strongly suggests that this process is a consequence of CO

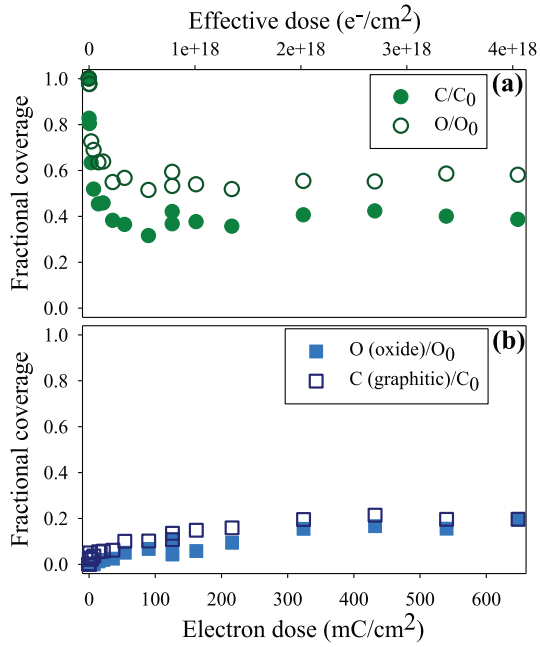

Figure 2. (a) Fractional coverage of total carbon (light green filled circles) and total oxygen species (dark green open circles). (b) Change in fractional coverage of graphitic carbon (dark blue open squares) and oxide species (light blue filled squares). Effective electron dose is expressed in units of mC/cm^2 (main axis) and e$^-$/cm^2 (top axis) for $Fe(CO)_5$ films exposed to 500 eV electrons.

desorption, consistent with previous studies of other metal carbonyls exposed to low energy electrons.[24,29−31,37] Figure 2b plots the relative abundance of graphitic carbon (open squares) and oxide oxygen (blue squares) upon irradiation with 500 eV electrons, as measured by the graphitic C(1s) and oxide O(1s) XPS peaks (Figure 1), respectively. These two species show a near identical kinetic dependence, indicating that they are likely produced by the same process and with equal efficiency. After an electron dose of ≈650 mC/cm^2, the graphitic carbon and oxide species represent about 20% of the original C(1s) or O(1s) signal, respectively, equivalent to ≈1 carbon or oxygen atom out of the original five CO ligands per $Fe(CO)_5$ molecule.

Examining Figures 1 and 2, it is evident that the electron-induced reactions of adsorbed $Fe(CO)_5$ proceed in two regimes, similar to other carbonyl-containing organometallic species.[29−31,37] The first regime, operative at electron doses < ≈ 20 mC/cm^2, is characterized primarily by the loss of CO ligands. This process which accompanies precursor decomposition can be described as

$$Fe(CO)_{5(ads)} + e^-(500eV) \xrightarrow{\sigma_1} Fe(CO)_{5-x(ads)} + xCO_{(g)} \uparrow \text{ precursor decomposition/CO desorption} \quad (1)$$

σ_1 is the total reaction cross section for the reaction described in eq 1, and x is the average number of CO ligands lost in this initial reaction step per $Fe(CO)_5$ molecule.. It is worth noting that the reaction cross sections discussed in this paper represent total reaction cross sections, measured for an incident electron of 500 eV or an Ar^+ energy of 1200 eV. These total cross sections represent the combined effects of not only the primary beam, but also the low energy secondary electrons generated by interactions of the primary beam with

https://doi.org/10.1021/acs.jpcc.1c05826
J. Phys. Chem. C 2021, 125, 17749−17760

the substrate.[10,49] The formula of the $Fe(CO)_{5-x(ads)}$ species represents a stoichiometric average of partially decarbonylated $Fe_y(CO)_z$ species produced in eq 1, rather than denoting a specific bonding structure. The reaction described in eq 1 is in line with previous studies which have proposed that low energy electron decomposition of $Fe(CO)_5$ thin films results in secondary reactions of anion fragments with neighboring $Fe(CO)_5$, leading to the production of heteronuclear, partially decarbonylated $Fe_n(CO)_m$ species and progressive CO elimination.[17,20,21]

The second reaction step in the $Fe(CO)_5$ films, which occurs predominantly at electron doses > ≈20 mC/cm^2, is characterized by decomposition of the CO ligands in the partially decarbonylated intermediates. In this regime, no carbon or oxygen is removed from the surface, with the XPS data indicating that residual CO ligands are decomposed into a graphitic carbon species and a reactive oxygen species, which oxidizes the iron. This set of reactions can therefore be described as

$$Fe(CO)_{5-x(ads)} + e^-(500eV) \xrightarrow{\sigma_2} FeO_{5-x(ads)} + (5-x)C_{(graphitic)} \text{ decomposition of CO ligands} \quad (2)$$

Here, σ_2 is the total reaction cross section for the reaction described in eq 2. The formula of the oxidized iron product ($FeO_{5-x(ads)}$) represents the mix of iron oxides and unoxidized iron species that remain on the surface. This process appears to be stoichiometric, evidenced by the constant oxygen and carbon signals observed by XPS during the electron-induced degradation of the partially decarbonylated intermediates (see Figure 2).The proposed mechanism for the electron-induced decomposition of adsorbed $Fe(CO)_5$—i.e., a two-step process consisting of an initial CO loss followed by decomposition of the remaining CO ligands has been proposed previously to explain the reactivity of many other metal carbonyls and carbonyl-containing organometallic precursors, including $Co(CO)_3NO$, $W(CO)_6$, $HFeCo_3(CO)_{12}$, $CpFe(CO)_2Mn(CO)_5$, and $CpFe(CO)_2Re(CO)_5$.[24,29−31,37]

In contrast to other metal carbonyls whose electron stimulated reactions have been studied by XPS, however, $Fe(CO)_5$ has only a single type of ligand (CO) and the C(1s) and O(1s) regions are reasonably well separated and therefore amenable to deconvolution into the different species (CO, graphitic carbon and oxide) present (see Figure 1). This facilitates the application of a kinetic model based on the two-step reaction sequence described in eqs 1 and 2. The full derivation of the equations used to determine the cross sections σ_1 and σ_2 and the associated fits to the experimental may be found in the Supporting Information; a brief summary is given here. In order to derive σ_1 from eq 1, we can start by writing the equation below:

$$\frac{[Fe(CO)_5]_D}{[Fe(CO)_5]_0} = e^{-\sigma_1 D} \quad (3)$$

Here, D is the electron dose, which may be given in mC/cm^2 or e$^-$/cm^2.

Since both carbon and oxygen are lost from the surface during the initial step (eq 1), but not during the second step (eq 2), total carbon or total oxygen coverage could each be used to determine the rate of $Fe(CO)_5$ loss from the surface. In our analysis, the total carbon coverage will be used, since Figure 1 shows that deconvolution into the different species (CO and C_{gr}) in the C(1s) region will be more accurate than the different species (CO and iron oxide) in the O(1s) region. As the initial carbon coverage is equal to five times the iron atom coverage and the latter is conserved during both eqs 1 and 2, we can show that

$$\frac{[C_{total}]_D}{[C_{total}]_0} = \frac{x}{5}e^{-\sigma_1 D} + \frac{5\text{-}x}{5} \quad (4)$$

where x is the number of CO ligands lost during the precursor decomposition/ligand loss step described in eq 1. Using eq 4, we can fit the total carbon loss as a function of electron dose to determine σ_1 and x. By this means, we determined a σ_1 value of 0.28 (±0.03) cm^2/mC (4.5×10^{-17} cm^2, 0.45 Å^2) and an x value of 2.9, the latter representing the average number of CO molecules lost per $Fe(CO)_5$ molecule during decomposition. The same analysis using the O(1s) region leads to an x value of 2.2. Consequently, we estimate than an average of 2.5 or 50% of the CO ligands desorb in the initial step.

We can determine σ_2 from the loss of CO and/or the growth of the graphitic C(1s) peak, which we can describe by the following equation based on eqs 1 and 2:

$$\frac{[C_{CO}]_D}{[C_{total}]_0} = \frac{5-x}{5}\left(\frac{\sigma_1}{\sigma_2-\sigma_1}+1\right)e^{-\sigma_1 D} + \frac{5-x}{5}\left(\frac{\sigma_1}{\sigma_2-\sigma_1}\right)e^{-\sigma_2 D} \quad (5)$$

$$\frac{[C_{graphitic}]_D}{[C_{total}]_0} = \frac{5\text{-}x}{5} - \frac{5\text{-}x}{5}\left(\frac{\sigma_1}{\sigma_2-\sigma_1}+1\right)e^{-\sigma_1 D} + \frac{5\text{-}x}{5}\left(\frac{\sigma_1}{\sigma_2-\sigma_1}\right)e^{-\sigma_2 D} \quad (6)$$

The analytical derivation of eq 6 is detailed in the Supporting Information. Using the previously determined x and σ_1 values, the graphitic carbon growth data was fit to find a σ_2 value of 0.0019 (±0.003) cm^2/mC (3.1×10^{-19} cm^2, 0.0034 Å^2), more than 2 orders of magnitude smaller than σ_1.

Figure 3 shows plots of total carbon loss (green filled circles), carbonyl carbon loss (red filled triangles), and graphitic carbon growth (blue filled squares) fitted using best fit values of x, σ_1 and σ_2 values determined from eqs 5 and 6. The model is seen to provide a good qualitative fit to the experimental data; deviations between the predictions of the kinetic model and the experimental data are most evident in the second step of the reaction. This reflects the simplicity of the equation used to describe the decomposition of the partially decarbonylated intermediates (eq 2). Notably, we can reasonably expect a range of σ_2 values given the presence of a heterogeneous mixture of ($Fe(CO)_{5-x(ads)}$) species, along with the likelihood that decomposition occurs via a sequential sequence of electron-stimulated reactions ($Fe(CO)_{5-x(ads)} + e^- \rightarrow Fe(CO)_{5-x-y} + e^- \rightarrow \rightarrow FeO_{(ads)} + C_{(ads)}$).

Our findings are in broad agreement with previous studies. For example, Henderson et al. observed that low-energy (3−132 eV) electrons induce the conversion of molecularly adsorbed $Fe(CO)_5$ into Fe(CO) clusters on Ag surfaces which are much resistant to further electron-induced reactions.[20] Hauchard also observed two sequential electron-induced reactions of adsorbed thin films of $Fe(CO)_5$[21] adsorbed at 45 K with a cross section for the first and second reaction of 270 Å^2 and 11.5 Å^2 respectively. However, the magnitudes of these cross sections are significantly higher than the σ_1 and σ_2

https://doi.org/10.1021/acs.jpcc.1c05826
J. Phys. Chem. C 2021, 125, 17749−17760

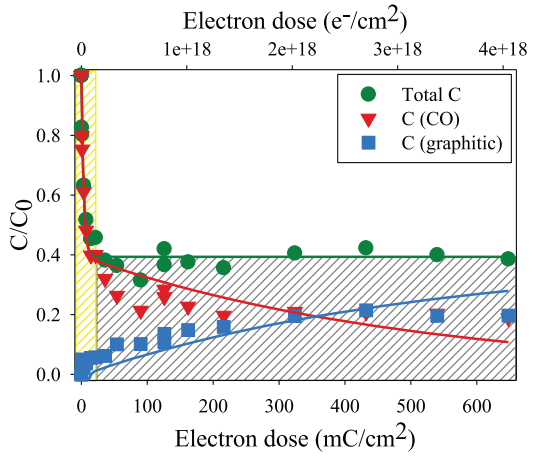

Figure 3. Kinetics of total carbon loss (green filled circles), carbonyl carbon loss (red filled triangles), and graphitic carbon growth (blue filled squares) fitted with eqs 4 (green line), 5 (red line), and 6 (blue line), respectively. The CO-loss area and the CO-decomposition area indicated with yellow and gray colored shaded rectangles, respectively. Effective electron dose is expressed in units of mC/cm^2 (main axis) and e$^-$/cm^2 (top axis).

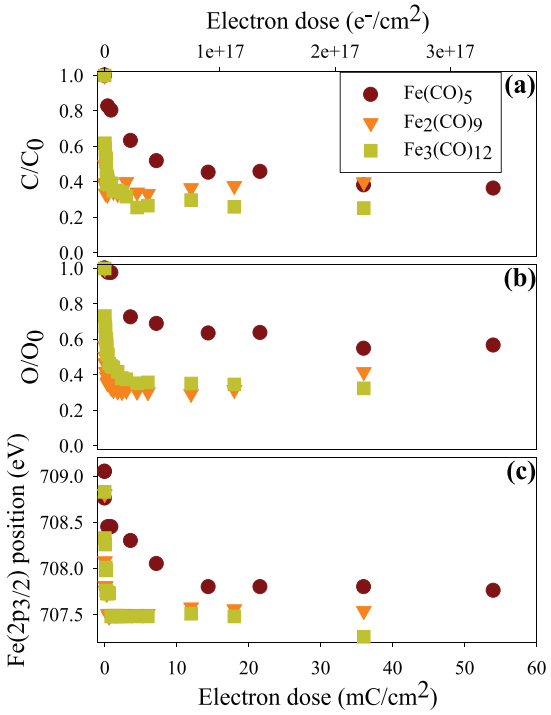

Figure 4. Comparison of relative abundance from $Fe(CO)_5$ (dark red circles), $Fe_2(CO)_9$ (orange triangle), and $Fe_3(CO)_{12}$ (dark yellow squares) of (a) total carbon, (b) total oxygen elements. (c) Change in $Fe(2p_{3/2})$ peak position for three iron carbonyl compounds. Effective electron dose is expressed in units of mC/cm^2 (main axis) and e$^-$/cm^2 (top axis).

cross sections derived from our kinetic analysis. Upon annealing $Fe(CO)_5$ films to 140 K and recooling to 45 K, Hauchard found that the $Fe(CO)_5$ film restructured as a result of aggregation. This restructuring massively decreased the sensitivity of the $Fe(CO)_5$ films to electron irradiation, reducing the reaction cross sections by 2−3 orders of magnitude. Thus, our observation of cross sections (σ_1 and σ_2) that are approximately 3 orders of magnitude lower than those reported by Hauchard aligns well with their values for the $Fe(CO)_5$ films annealed to 140 K. The suppression of reactivity in $Fe(CO)_5$ aggregates is also consistent with the suppression of DI in $Fe(CO)_5$ clusters discussed in previous studies,[14,17] although in isolation our studies do not provide a means to identify the mechanism of precursor decomposition. Our XPS data also does not provide a means to identify and quantify any charged particles which desorb during electron irradiation, although the ability of our kinetic model to provide a good qualitative fit to the experimental data implies that the relative concentration of such species in small.

Figure S2 shows the changes in the C(1s), O(1s), and Fe(2p) regions of $Fe_2(CO)_9$ and $Fe_3(CO)_{12}$ thin films that occur as a result of exposure to 500 eV electrons, while Figure S3 demonstrates that these changes are the result of electron exposure and not X-ray irradiation The spectroscopic changes in Figure S2 are seen to mirror those observed for $Fe(CO)_5$ suggesting a similar sequence of reactions. Parts a and b of Figure 4 plot a comparison of the rate of loss of carbon and oxygen from $Fe(CO)_5$, $Fe_2(CO)_9$, and $Fe_3(CO)_{12}$ thin films as a function of the electron dose. What is notable is that although the extent of CO desorption is comparable for all three iron carbonyls the rate of CO desorption is significantly larger (approximately 1 order of magnitude) for $Fe_2(CO)_9$ and $Fe_3(CO)_{12}$ as compared to $Fe(CO)_5$. This increase in reactivity is consistent with previous studies of bimetallic organometallic complexes[30] and in part is a consequence of the larger size of these polynuclear organometallic complexes, which leads to a larger effective reaction-cross section. However, the magnitude of the difference in reactivity suggests that other factors may also be present. Figure 4c compares the change in Fe ($2p_{3/2}$) peak position for the three iron carbonyls. In each case electron irradiation causes a decrease in Fe binding energy at a rate commensurate with the desorption of CO. For each carbonyl complex, the binding energy plateaus at a value of ≈707.5 eV, intermediate between the binding energy of the parent metal carbonyl and metallic iron (≈706.6 eV[50]).

Reactions with Low Energy Ar$^+$. Figure 5 shows the evolution of the C(1s), O(1s), and Fe(2p) XPS regions of a $Fe(CO)_5$ thin film (1.8 nm) upon exposure to 1200 eV Ar$^+$. The effective dose is given in mC/cm^2. The spectra of the as-deposited $Fe(CO)_5$ films, shown at the bottom of each region, are similar to those described previously in Figure 1. Upon 1200 eV Ar$^+$ irradiation the main CO C(1s) peak at 287.7 eV and the $\pi-\pi^*$ shakeup peak at 293.2 eV (both shown as red curves in Figure 5) rapidly decrease in intensity, while a lower binding energy peak at approximately 283.7 eV (shown as blue curves in Figure 5) appears. Although this peak position is lower than the value typically observed for graphitic carbon (284.0−284.5 eV), it is still significantly higher than values assigned to iron carbide (≈ 283 eV).[51] Thus, on balance, the experimental data is more suggestive of graphitic carbon. After 0.22 mC/cm^2 of Ar$^+$ exposure, the CO peaks have all but disappeared and the C(1s) region is composed almost exclusively of graphitic carbon. For more prolonged Ar$^+$ irradiation this graphitic carbon peak slowly decreases in intensity until almost of the carbon-containing species have been removed after an Ar$^+$ dose of 0.99 mC/cm^2.

Changes in the O(1s) region upon 1200 eV Ar$^+$ exposure are characterized solely by a systematic decrease in the CO peak intensity and in marked contrast to electron irradiation, no measurable oxide O(1s) peak is observed. The evolution of the

https://doi.org/10.1021/acs.jpcc.1c05826
J. Phys. Chem. C 2021, 125, 17749−17760

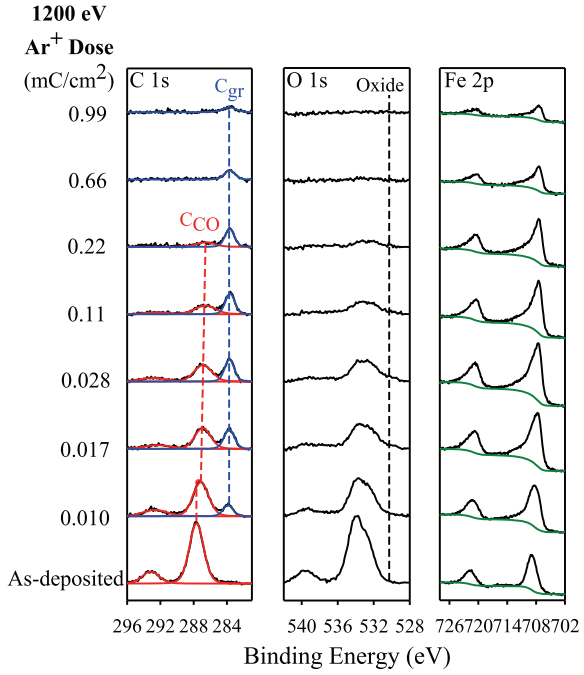

Figure 5. Evolution of the C(1s), O(1s), and Fe(2p) XPS regions of ≈1.8 nm thin film of $Fe(CO)_5$ upon irradiation with 1200 eV argon ions. The bottom spectra represent the unirradiated film. Speciation is shown in the C(1s) region, where the red line represents the C(1s) peak associated with the precursor carbonyl ligands while the blue lines represent the C(1s) peak associated with the graphitic carbon species in the deposit. The green curves in the Fe(2p) region shows the background. Ion dose is shown on the left-hand side in units of mC/cm^2.

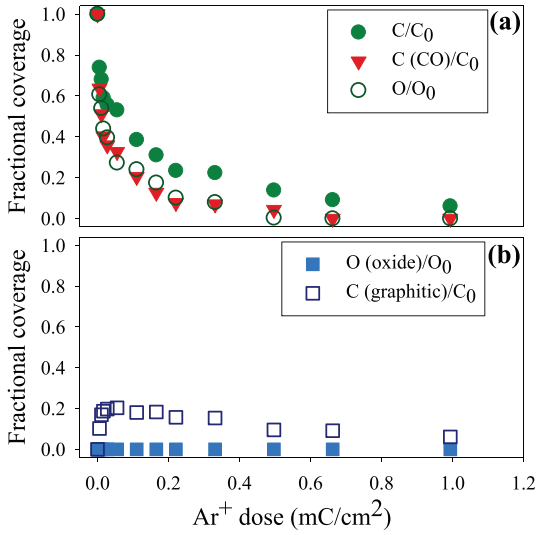

Figure 6. (a) Changes in total carbon coverage (green filled circles), carbonyl carbon coverage (filled red triangles), and total oxygen coverage oxygen coverage (green open circles) and (b) fractional coverage of graphitic carbon (dark blue open squares) and oxide species (light blue filled squares) upon exposure of ≈1.8 nm thin film of $Fe(CO)_5$ to 1200 eV Ar^+.

Fe(2p) region also differs substantially from the changes observed upon electron irradiation (compare Figures 1 and 5). Most significantly, there is no evidence of discernible new features at higher binding energies indicative of iron oxide formation, but rather just an increase in the high binding energy tail of the Fe(2p) peaks and a decrease in the $Fe(2p_{3/2})$ peak position from 708.8 to 707.5 eV, to a profile indicative of a metallic Fe.[46] This assertion is supported by the observation that this Fe(2p) spectral profile is retained at Ar^+ doses when all oxygen and almost all carbon atoms have been removed. It should be noted that, for argon doses higher than 0.028 mC/cm^2, Figure 5 shows iron atoms are removed from the surface.

Figure 6a shows the change in the fractional coverage of carbon (green circles) and oxygen (open circles) atoms as a function of 1200 eV Ar^+ dose; for carbon the fraction change in carbonyl (CO) carbon is also shown (filled red triangles). The fractional change in total oxygen coverage (open circles) overlaps with the carbonyl carbon atom coverage (filled red triangles), supporting the idea that all oxygen-containing species observed during Ar^+ irradiation are associated with CO and no oxides are formed. Figure S4 shows the corresponding changes in the XPS profiles and speciation when the Ar^+ energy is increased to 3000 eV. All of the various changes observed are analogous to the ones observed at 1200 eV, except that they occur at a different rate.

Figure 6b shows the fractional coverage of graphitic carbon (open squares) and oxide species (closed light blue squares) as measured by the respective C(1s) and O(1s) XPS peaks in Figure 5, plotted as a function of 1200 eV Ar^+ dose. Upon irradiation the fractional coverage of graphitic carbon rapidly increases until a maximum value of ≈0.2 is reached after an Ar^+ dose of 0.028 mC/cm^2, a dose that corresponds to the loss of approximately 60% of the CO groups from the $Fe(CO)_5$ film. For Ar^+ exposures in excess of 0.028 mC/cm^2 the graphitic carbon undergoes a slow but steady decrease in coverage (see Figure 5), ascribed to Ar^+ sputtering. Ar^+ exposures in excess of 0.028 mC/cm^2 also lead to a decrease in Fe atom coverage, but at a noticeably slower rate than carbon. No evidence of any iron oxide formation is observed throughout the entire reaction.

If we compare the effect of electron and Ar^+ irradiation on $Fe(CO)_5$ films a number of similarities, but more significant differences are apparent. These similarities and differences are most clearly discerned by comparing Figures 2 and 6. While both electron and ion exposures lead to CO desorption, the extent of CO loss is significantly higher during ion beam irradiation. Specifically, electron irradiation leads to on average about half (~50%) of the nascent CO ligands undergoing desorption while ion irradiation is responsible for approximately 80% CO desorption. Graphitic carbon is formed during both ion and electron irradiation and reaches a similar maximum fractional coverage of ≈0.2. However, during electron irradiation the formation of graphitic carbon increases slowly and steadily over the course of the reaction, while for ion irradiation graphitic carbon is formed rapidly during the earliest stages of the reaction and thereafter slowly decreases in coverage. During electron irradiation, iron oxides are formed concomitantly with formation of graphitic carbon, while no evidence of iron oxidation is observed during ion bombardment, only sputtering of the metallic iron after longer periods of ion bombardment. Thus, it is evident that the effects of ion bombardment are not dominated by reactions of secondary electron generated by ion−substrate interactions, in which case the effects of electron and ion irradiation would be largely similar.

Examining Figures 5 and 6 together, we hypothesize that the ion-induced reactions with adsorbed thin films of $Fe(CO)_5$

https://doi.org/10.1021/acs.jpcc.1c05826
J. Phys. Chem. C 2021, 125, 17749−17760

proceeds via the following two sequential elementary reaction steps:

$$Fe(CO)_{5(ads)} + Ar^+ \xrightarrow{\sigma_3} Fe_{(ads)} + (5-n)C_{(ads)} + nCO_{(g)} \uparrow \text{(precursor decomposition)} \quad (7)$$

$$(5-n)C_{(ads)} + Fe_{(ads)} + Ar^+ \xrightarrow{\sigma_4} C_{(g)} + Fe_{(g)} \text{ (sputtering of deposited atoms)} \quad (8)$$

In the first step, an impulsive collision leads to energy transfer from Ar^+ to adsorbed $Fe(CO)_5$ molecules and complete fragmentation/decomposition of the precursor. The idea that energy transfer from an incoming 1200 eV Ar^+ to an adsorbed $Fe(CO)_5$ molecule is sufficient to initiate complete desorption/decomposition of all 5 CO ligands is supported by a determination that the maximum energy transfer that could occur in such a kinematic collision is 676 eV, much greater than the CO and Fe-CO bond strengths (≈11 eV and ≈1.5 eV).[12,22,52] CO liberated in this step desorbs, giving rise to the concurrent loss of peak intensity within both the C(1s) and O(1s) XPS regions associated with carbonyl species (see Figure 5). However, some fraction of the CO ligands undergo decomposition as opposed to desorption, producing graphitic carbon. Although the identity of the oxygen species liberated during ion-induced CO decomposition is unclear, it is evident that these oxygen species desorb rather than causing iron oxidation.

The second reaction step involves the physical sputtering of the graphitic carbon and iron produced by ion-induced fragmentation of the precursor, providing a rationale for the loss of intensity in the Fe(2p) region and the loss of graphitic carbon in the C(1s) region after prolonged periods of Ar^+ bombardment. The fate of the oxygen atoms liberated during CO decomposition is unclear. Although it is possible that they react with iron to form an oxide before the oxygen is rapidly sputtered, it seems most likely that oxygen is ejected into the gas phase during the CO decomposition step, possibly as ions.

It is also worth noting that in common with two recent studies where we have investigated low energy ion reactions with adsorbed organometallic precursors,[37,53] the significant chemical transformations to $Fe(CO)_5$ observed in the form of CO desorption and decomposition, occur in the absence of any measurable molecular desorption, despite the fact that the $Fe(CO)_5$ molecules are only bound to the substrate through comparatively weak physisorption interactions. Experimentally, the absence of ion-induced $Fe(CO)_5$ desorption is evident in Figure 5 by the absence of a decrease in the Fe XPS signal during the initial stages of Ar^+ bombardment when $Fe(CO)_5$ molecules are undergoing ion-induced decomposition. This suggests that, during Ar^+ collisions with $Fe(CO)_5$, not only is energy efficiently transferred from the ion to the precursor but also the subsequent intermolecular energy transfer, which leads to molecular decomposition, occurs before energy is transferred to the adsorbate−substrate bond.

Based on the two-step kinetic model of precursor decomposition followed by sputtering suggested by our experimental data, we can describe the decrease in coverage of $Fe(CO)_5$ molecules ($[Fe(CO)_5]_D$), as a first order loss process, which based on reaction 7 will be proportional to the CO coverage. Accounting for the Gaussian intensity of ions produced by the ion gun[54] this will lead to the following equation (see Supporting Information for details):

$$\frac{[Fe(CO)_5]_D}{[Fe(CO)_5]_{D=0}} = \frac{[CO_{(ads)}]_D}{[CO_{(ads)}]_{D=0}} = \frac{(1-e^{-bD})}{bD} \quad (9)$$

Figure 7 shows the fractional CO coverage ($[CO_{(ads)}]_D/[CO_{(ads)}]_{D=0}$) plotted as a function of the ion dose (D), along

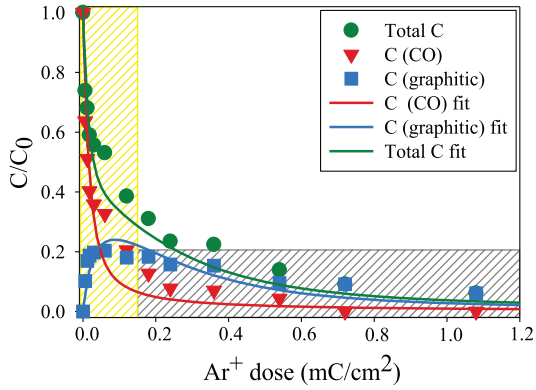

Figure 7. Kinetics of total carbon loss (green filled circles), carbonyl carbon loss (red filled triangles), and graphitic carbon growth (blue filled squares) fitted with eqs 7 (red line) and 8 (blue line) and the sum of eqs 7 and 8 (green line) respectively. The CO-loss area and the $C_{(ads)}$-sputtering area indicated with yellow and gray colored shaded rectangles, respectively. Ion exposure is expressed in units of dose (mC/cm^2).

with the red line which represents the best-fit line to the CO (and by inference the $Fe(CO)_5$) coverage, based on eq 9. The prediction of eq 9 is seen to be in qualitatively good agreement with the experimentally observed data with b = 110 (±15) cm^2/mC. Using eqs 7 and 8, the fractional coverage of graphitic carbon (ratioed to the initial carbon coverage) can be described by the following kinetic equation;

$$\frac{d[C_{ads}]_D}{dD} = \left(\frac{5-n}{n}\right)(\sigma_3[Fe(CO)_5]_D - \sigma_4[C_{ads}]_D) \quad (10)$$

Note that to simplify the math and generate a solvable analytical solution the sputtering rate of graphitic carbon was assumed to be occur with a uniform spatial flux of ions. The analytical solution of eq 10, along with the best fit values of σ_3 and σ_4 are described in eqs S18 and S19 in the Supporting Information. The best fit line through the experimentally determined values of $C_{(ads)}$ generated by eq 8 is plotted as the solid blue line in Figure 7 and is in qualitative agreement with the experimental data. Similarly, the total carbon coverage (shown as a solid green line), calculated by adding the best fit values for the fractional coverages of $CO_{(ads)}$ and $C_{(ads)}$ together, is seen to agree well with the experimental variation in total carbon atom coverage. In addition to providing support for the mechanism proposed in reactions (7) and (8), results from this kinetic analysis reveal that approximately one out of every five CO molecules in the precursor undergoes decomposition rather than desorption, and the rate of ion-induced precursor decomposition is at least an order of magnitude greater than the subsequent ion-induced sputtering of the graphitic carbon produced as a result of $Fe(CO)_5$ decomposition.

The sequential steps of electron- and Ar^+-induced reactions, proposed in eqs 1, 2, 7, and 8, are schematically illustrated in Figure 8.

https://doi.org/10.1021/acs.jpcc.1c05826
J. Phys. Chem. C 2021, 125, 17749−17760

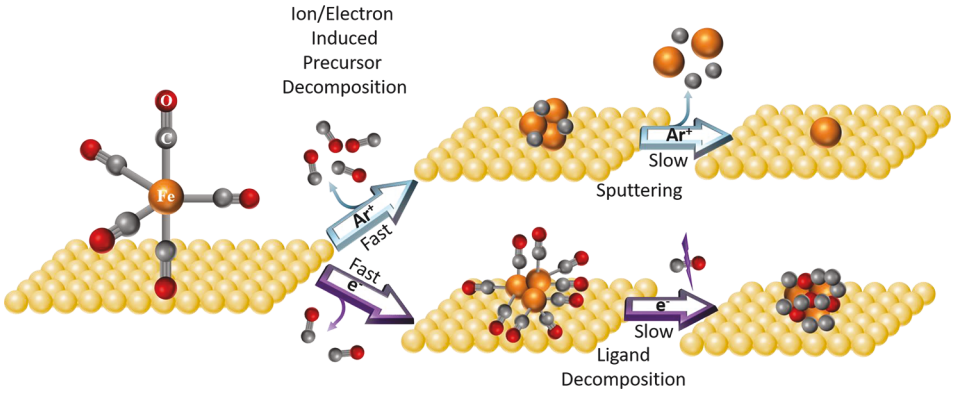

Figure 8. Schematic representation of the reaction steps that accompanied by the 1200 eV Ar^+ (top) and 500 eV electron (bottom) exposure of adsorbed $Fe(CO)_5$ on a gold substrate.

Results contained in the present study can be compared to the recently reported fragmentation of gas phase $Fe(CO)_5$ using 3 keV Ar^+,[22] recognizing that gas phase studies have relevance to the initial ion-induced precursor decomposition step reported herein. Some qualitative similarities are apparent, perhaps most notably the significant degree of fragmentation and CO loss observed in both studies, with $Fe(CO)^+$ and Fe^+ being the dominant peaks in the gas phase study, along with smaller contributions from $Fe(CO)_2^+$ and FeC^+. However, the extent of CO desorption and decomposition are both more pronounced in the surface science studies, although it should be noted that the gas phase study was limited to the detection of charged fragments by mass spectrometry. One notable finding from the gas phase studies is the different reactivity ascribed to the effect of He^+ on $Fe(CO)_5$ molecules, where interactions were indicative of electronic excitation and noticeably lower fragmentation efficiencies. Given the increasing use of He^+ for creating nanostructues[55−59] it would therefore be interesting to study the effects of He^+ on adsorbed $Fe(CO)_5$ to see if significantly different fragmentation patterns were observed and if the effects of He^+ at least in the initial precursor decomposition step, bore more of a resemblance to the effects of low energy electrons.

Broadly speaking the difference in electron- and ion-induced reactions are similar to the findings of our recent study of $(\eta^5\text{-Cp})Fe(CO)_2Re(CO)_5$, where low energy Ar^+ bombardment led to a much higher degree of ligand fragmentation in the form of CO desorption during precursor decomposition as compared to electron irradiation.[37] Similarly, Ar^+-induced fragmentation was followed by preferential sputtering of the residual organic species rather than the deposited metal atoms, while sustained electron irradiation caused ligand decomposition. One notable difference, however, is evidence for Ar^+-induced CO dissociation in the present study which was not observed for $(\eta^5\text{-Cp})Fe(CO)_2Re(CO)_5$.[37] The extent to which this difference is specific to the precursors in question or reflects more generalizable differences between classes of precursors remains to be determined. This question will likely be resolved as data from new low energy ion studies with other organometallic complexes emerges.

RELEVANCE TO FEBID AND FIBID

The present investigation is relevant to the creation of nanostructures from $Fe(CO)_5$ using electrons (FEBID) or ions (FIBID) where deposits are created under steady state deposition conditions and the growth surface is at or slightly above room temperature.[1,2,4,5,9] In the case of FIBID, our data indicate that the nonvolatile products of precursor decomposition will be a roughly equal concentration of iron and carbon atoms. These species will become incorporated into the deposit as described in Figure 8(top). Under conditions of comparatively high precursor flux, subsequent ion reactions with the growth surface will initiate further deposition due to ion-induced decomposition of adsorbed $Fe(CO)_5$ molecules. In contrast, in a precursor limited regime sputtering of adsorbed carbon (and to a lesser extent Fe) will predominate. Indeed, analysis of Figure 5 reveals that an appropriate choice of deposition conditions could yield purely metallic Fe deposits. These insights will be useful to understand and rationalize the composition of nanostructures if and when they are created from $Fe(CO)_5$ using FIBID.

In contrast to FIBID, $Fe(CO)_5$ has been widely used as a precursor in FEBID.[2,4,5] Our data indicates that the initial step, summarized in Figure 8(bottom), in the FEBID process will be the desorption of approximately half of the CO ligands (~2.5), accompanied by the formation of a partially decarbonylated intermediate which will become incorporated into the growth surface as part of the deposit, as shown in Figure 8(bottom). Further electron-induced reactivity will cause the residual CO groups to decompose, forming graphitic carbon and iron oxide. However, analysis of the FEBID literature reveals that the typical composition of deposits created from $Fe(CO)_5$ exhibit metal concentrations >50%,[1,2,4] much higher that would be predicted from this investigation. The discrepancy arises from the difference in substrate temperatures. In the present study thermal and catalytic reactions of intermediates are hindered by the low (200 K) substrate temperature. However, separate experiments (data not shown), consistent with prior work by Henderson et al.,[20] indicate that at room temperature the partially decarbonylated intermediates undergo thermal decomposition leading to CO desorption. Thus, during FEBID, the following reaction sequence can occur:

$$Fe(CO)_{5(ads)} + e^-(500\ eV) \xrightarrow{\sigma_1} Fe(CO)_{5-x(ads)} + xCO_{(g)}\uparrow \quad (11)$$

$$Fe(CO)_{5-x(ads)} + \Delta \rightarrow Fe_{(ads)} + (5-x)CO_{(g)}\uparrow \quad (12)$$

Consequently, under steady state deposition conditions where the substrate is at room temperature, partially decarbonylated intermediates can undergo either electron-beam-induced decomposition (producing iron oxides) or thermal desorption (producing iron), depending on the

https://doi.org/10.1021/acs.jpcc.1c05826
J. Phys. Chem. C 2021, 125, 17749−17760

deposition conditions (most importantly the electron vs precursor flux). Given the inertness of the partially decarbonylated intermediates to electron-induced decomposition ($\sigma_2 \ll \sigma_1$) it is to be anticipated that CO desorption via eq 12 will be the most likely reaction pathway for the partially decarbonylated intermediates under most deposition conditions. This explains why the iron content in FEBID studies is higher than would be predicted from the UHV surface science results described herein and also helps to explain the different compositions reported in different studies.[1,2,4,5]

CONCLUSIONS

Low energy electron irradiation of $Fe(CO)_5$ films adsorbed at 200 K under UHV conditions causes precursor decomposition, and in the process, an average ~2.5 CO molecules per molecule desorb, forming a partially decarbonylated overlayer with a stoichiometry of ~ $Fe(CO)_{2.5}$. Upon further irradiation, electron-induced decomposition of the residual CO ligands ($CO_{(ads)} \rightarrow C_{(ads)} + O_{(ads)}$) within the partially decarbonylated overlayer occurs, producing oxidized iron atoms embedded in a graphitic carbonaceous matrix. The rate of this second step is, however, at least an order of magnitude slower than the initial precursor decomposition step. These findings are in broad agreement with previous studies of $Fe(CO)_5$ thin films and the general reactivity pattern observed for other metal carbonyls exposed to electron irradiation. $Fe_2(CO)_9$ and $Fe_3(CO)_{12}$ reacted similarly to $Fe(CO)_5$ in terms of the two-step reaction sequence (CO desorption followed by CO decomposition), although the initial rate of precursor decomposition was significantly higher, an effect attributed in part to the larger cross-sectional area of these polynuclear iron carbonyls. During FEBID, thermal desorption of CO will compete with electron-induced decomposition of CO ligands from the partially decarbonylated overlayer, providing a rationale for the higher metal contents observed in traditional FEBID studies using iron carbonyls, as compared to the predictions of a process determined exclusively by electron-induced reactions. In contrast to electrons, $Fe(CO)_5$ molecules undergo complete fragmentation during their exposure to low energy (1200 eV) Ar^+. This process leads to desorption of an average of four CO ligands per precursor molecule, along with the decomposition of one CO ligand to produce graphitic carbon and a reactive oxygen species which desorbs. The residual iron and carbon atoms are subsequently subject to ion-induced sputtering, with a preferential loss of the organic species to produce a purely metallic film.

ASSOCIATED CONTENT

Supporting Information

The Supporting Information is available free of charge at https://pubs.acs.org/doi/10.1021/acs.jpcc.1c05826.

Section S1, derivation of kinetic equations to rationalize XPS data observed upon electron irradiation; Section S2, derivation of kinetic equations to rationalize XPS data observed upon Ar^+ exposure; Figure S1, XPS regions for C(1s), O(1s), and Fe(2p) irradiated with Mg Kα X-rays; Figure S2, XPS data for $Fe_2(CO)_9$ (left) and $Fe_3(CO)_{12}$ (right) upon irradiation with 500 eV electrons; Figure S3, XPS data for$Fe_2(CO)_9$ (left) and $Fe_3(CO)_{12}$ (right) upon irradiation with Mg Kα X-rays; Figure S4, XPS data for $Fe(CO)_5$ upon irradiation with 3000 eV argon ions; and Figure S5, C and O coverages and peak positions upon 3000 eV Ar^+ bombardment of an $Fe(CO)_5$ film (PDF)

AUTHOR INFORMATION

Corresponding Author

D. Howard Fairbrother − *Department of Chemistry, Johns Hopkins University, Baltimore, Maryland 21218-2685, United States;* orcid.org/0000-0003-4405-9728; Email: howardf@jhu.edu

Authors

Elif Bilgilisoy − *Physikalische Chemie II, Friedrich-Alexander Universität Erlangen-Nürnberg, 91058 Erlangen, Germany*

Rachel M. Thorman − *Department of Chemistry, Johns Hopkins University, Baltimore, Maryland 21218-2685, United States*

Michael S. Barclay − *Department of Chemistry, Johns Hopkins University, Baltimore, Maryland 21218-2685, United States*

Hubertus Marbach − *Physikalische Chemie II, Friedrich-Alexander Universität Erlangen-Nürnberg, 91058 Erlangen, Germany;* orcid.org/0000-0002-1982-9690

Complete contact information is available at: https://pubs.acs.org/10.1021/acs.jpcc.1c05826

Notes

The authors declare no competing financial interest.

ACKNOWLEDGMENTS

D.H.F. thanks the National Science Foundation for supporting this work through Grants CHE-1607621 and CHE-1904559. This work was conducted within the framework of ELENA, a European Union's Horizon 2020 research and innovation program under the Marie Skłodowska-Curie Grant Agreement No. 722149. E.B. and H.M. acknowledge financial support by the Deutsche Forschungsgemeinschaft (DFG) within the research unit FOR 1878/funCOS.

REFERENCES

(1) De Teresa, J.; Fernández-Pacheco, A.; Córdoba, R.; Serrano-Ramón, L.; Sangiao, S.; Ibarra, M. R. Review of magnetic nanostructures grown by focused electron beam induced deposition (FEBID). *J. Phys. D: Appl. Phys.* **2016**, *49*, 243003.

(2) Utke, I.; Hoffmann, P.; Melngailis, J. Gas-assisted focused electron beam and ion beam processing and fabrication. *J. Vac. Sci. Technol., B: Microelectron. Nanometer Struct. Process., Meas., Phenom* **2008**, *26*, 1197−1276.

(3) Melngailis, J. Focused ion beam technology and applications. *J. Vac. Sci. Technol., B: Microelectron. Process. Phenom.* **1987**, *5*, 469−495.

(4) Gavagnin, M.; Wanzenboeck, H. D.; Shawrav, M. M.; Belic, D.; Wachter, S.; Waid, S.; Stoeger-Pollach, M.; Bertagnolli, E. Focused electron beam-induced CVD of iron: a practical guide for direct writing. *Chem. Vap. Deposition* **2014**, *20*, 243−250.

(5) Lukasczyk, T.; Schirmer, M.; Steinrück, H. P.; Marbach, H. Electron-beam-induced deposition in ultrahigh vacuum: lithographic fabrication of clean iron nanostructures. *Small* **2008**, *4*, 841−846.

(6) Bruk, M.; Zhikharev, E.; Grigor'ev, E.; Spirin, A.; Kal'nov, V.; Kardash, I. Focused electron beam-induced deposition of iron-and carbon-containing nanostructures from triiron dodecacarbonyl vapor. *High Energy Chem.* **2005**, *39*, 65−68.

(7) Rodríguez, L. A.; Deen, L.; Córdoba, R.; Magén, C.; Snoeck, E.; Koopmans, B.; De Teresa, J. M. Influence of the shape and surface oxidation in the magnetization reversal of thin iron nanowires grown by focused electron beam induced deposition. *Beilstein J. Nanotechnol.* **2015**, *6*, 1319−1331.

(8) Takeguchi, M.; Shimojo, M.; Mitsuishi, K.; Tanaka, M.; Che, R.; Furuya, K. Fabrication of nanostructures with different iron concentration by electron beam induced deposition with a mixture gas of iron carbonyl and ferrocene, and their magnetic properties. *J. Mater. Sci.* **2006**, *41*, 4532−4536.
(9) Kubena, R.; Stratton, F.; Mayer, T. Selective area nucleation for metal chemical vapor deposition using focused ion beams. *J. Vac. Sci. Technol., B: Microelectron. Process. Phenom.* **1988**, *6*, 1865−1868.
(10) Thorman, R. M.; Kumar, T. P. R.; Fairbrother, D. H.; Ingólfsson, O. The role of low-energy electrons in focused electron beam induced deposition: four case studies of representative precursors. *Beilstein J. Nanotechnol.* **2015**, *6*, 1904−1926.
(11) Allan, M.; Lacko, M.; Papp, P.; Matejčík, Š.; Zlatar, M.; Fabrikant, I. I.; Kočišek, J.; Fedor, J. Dissociative electron attachment and electronic excitation in $Fe(CO)_5$. *Phys. Chem. Chem. Phys.* **2018**, *20*, 11692−11701.
(12) Lacko, M.; Papp, P.; Wnorowski, K.; Matejčík, Š. Electron-induced ionization and dissociative ionization of iron pentacarbonyl molecules. *Eur. Phys. J. D* **2015**, *69*, 1−9.
(13) Lengyel, J.; Papp, P.; Matejčík, Š.; Kočišek, J.; Fárník, M.; Fedor, J. Suppression of low-energy dissociative electron attachment in $Fe(CO)_5$ upon clustering. *Beilstein J. Nanotechnol.* **2017**, *8*, 2200−2207.
(14) Lengyel, J.; Fedor, J.; Fárník, M. Ligand stabilization and charge transfer in dissociative ionization of $Fe(CO)_5$ aggregates. *J. Phys. Chem. C* **2016**, *120*, 17810−17816.
(15) Lengyel, J.; Pysanenko, A.; Swiderek, P.; Heiz, U.; Fárník, M.; Fedor, J. Water-assisted electron-induced chemistry of the nanofabrication precursor iron pentacarbonyl. *J. Phys. Chem. A* **2021**, *125*, 1919−1926.
(16) Compton, R.; Stockdale, J. Formation of gas-phase negative ions in $Fe(CO)_5$ and $Ni(CO)_4$. *Int. J. Mass Spectrom. Ion Phys.* **1976**, *22*, 47−55.
(17) Massey, S.; Bass, A. D.; Sanche, L. o. Role of low-energy electrons (< 35 eV) in the degradation of $Fe(CO)_5$ for focused electron beam induced deposition applications: study by electron stimulated desorption of negative and positive ions. *J. Phys. Chem. C* **2015**, *119*, 12708−12719.
(18) Lengyel, J.; Kočišek, J.; Fárník, M.; Fedor, J. Self-scavenging of electrons in $Fe(CO)_5$ aggregates deposited on argon nanoparticles. *J. Phys. Chem. C* **2016**, *120*, 7397−7402.
(19) Foord, J.; Jackman, R. Studies of adsorption and electron-induced dissociation of $Fe(CO)_5$ on Si (100). *Surf. Sci.* **1986**, *171*, 197−207.
(20) Henderson, M.; Ramsier, R.; Yates, J., Jr Low-energy electron induced decomposition of $Fe(CO)_5$ adsorbed on Ag (111). *Surf. Sci.* **1991**, *259*, 173−182.
(21) Hauchard, C.; Rowntree, P. A. Low-energy electron-induced decarbonylation of $Fe(CO)_5$ films adsorbed on Au (111) surfaces. *Can. J. Chem.* **2011**, *89*, 1163−1173.
(22) Indrajith, S.; Rousseau, P.; Huber, B. A.; Nicolafrancesco, C.; Domaracka, A.; Grygoryeva, K.; Nag, P.; Sedmidubská, B.; Fedor, J.; Kočišek, J. Decomposition of iron pentacarbonyl induced by singly and multiply charged ions and implications for focused ion Beam-induced deposition. *J. Phys. Chem. C* **2019**, *123*, 10639−10645.
(23) Wnorowski, K.; Stano, M.; Matias, C.; Denifl, S.; Barszczewska, W.; Matejčík, Š. Low-energy electron interactions with tungsten hexacarbonyl−$W(CO)_6$. *Rapid Commun. Mass Spectrom.* **2012**, *26*, 2093−2098.
(24) Rosenberg, S. G.; Barclay, M.; Fairbrother, D. H. Electron induced reactions of surface adsorbed tungsten hexacarbonyl ($W(CO)_6$). *Phys. Chem. Chem. Phys.* **2013**, *15*, 4002−4015.
(25) Landheer, K.; Rosenberg, S. G.; Bernau, L.; Swiderek, P.; Utke, I.; Hagen, C. W.; Fairbrother, D. H. Low-energy electron-induced decomposition and reactions of adsorbed tetrakis (trifluorophosphine) platinum [$Pt(PF_3)_4$]. *J. Phys. Chem. C* **2011**, *115*, 17452−17463.
(26) Spencer, J. A.; Brannaka, J. A.; Barclay, M.; McElwee-White, L.; Fairbrother, D. H. Electron-induced surface reactions of η^3-allyl ruthenium tricarbonyl bromide [$(\eta^3\text{-}C_3H_5)Ru(CO)_3Br$]: Contrasting the behavior of different ligands. *J. Phys. Chem. C* **2015**, *119*, 15349−15359.
(27) Spencer, J. A.; Wu, Y.-C.; McElwee-White, L.; Fairbrother, D. H. Electron induced surface reactions of cis-$Pt(CO)_2Cl_2$: A route to focused electron beam induced deposition of pure Pt nanostructures. *J. Am. Chem. Soc.* **2016**, *138*, 9172−9182.
(28) P, R. K. T.; Weirich, P.; Hrachowina, L.; Hanefeld, M.; Bjornsson, R.; Hrodmarsson, H. R.; Barth, S.; Fairbrother, D. H.; Huth, M.; Ingólfsson, O. Electron interactions with the heteronuclear carbonyl precursor $H_2FeRu_3(CO)_{13}$ and comparison with $HFeCo_3(CO)_{12}$: from fundamental gas phase and surface science studies to focused electron beam induced deposition. *Beilstein J. Nanotechnol.* **2018**, *9*, 555−579.
(29) Rosenberg, S. G.; Barclay, M.; Fairbrother, D. H. Electron beam induced reactions of adsorbed cobalt tricarbonyl nitrosyl ($Co(CO)_3NO$) molecules. *J. Phys. Chem. C* **2013**, *117*, 16053−16064.
(30) TP, R. K.; Unlu, I.; Barth, S.; Ingólfsson, O.; Fairbrother, D. H. Electron induced surface reactions of $HFeCo_3(CO)_{12}$, a bimetallic precursor for focused electron beam induced deposition (FEBID). *J. Phys. Chem. C* **2018**, *122*, 2648−2660.
(31) Unlu, I.; Spencer, J. A.; Johnson, K. R.; Thorman, R. M.; Ingólfsson, O.; McElwee-White, L.; Fairbrother, D. H. Electron induced surface reactions of $(\eta^5\text{-}C_5H_5)Fe(CO)_2Mn(CO)_5$, a potential heterobimetallic precursor for focused electron beam induced deposition (FEBID). *Phys. Chem. Chem. Phys.* **2018**, *20*, 7862−7874.
(32) Dubner, A.; Wagner, A.; Melngailis, J.; Thompson, C. The role of the ion-solid interaction in ion-beam-induced deposition of gold. *J. Appl. Phys.* **1991**, *70*, 665−673.
(33) Chen, P.; Salemink, H. W.; Alkemade, P. F. Roles of secondary electrons and sputtered atoms in ion-beam-induced deposition. *J. Vac. Sci. Technol., B: Microelectron. Nanometer Struct. Process., Meas., Phenom* **2009**, *27*, 2718−2721.
(34) Ro, J.; Thompson, C.; Melngailis, J. Mechanism of ion beam induced deposition of gold. *J. Vac. Sci. Technol., B: Microelectron. Process. Phenom.* **1994**, *12*, 73−77.
(35) Lipp, S.; Frey, L.; Lehrer, C.; Demm, E.; Pauthner, S.; Ryssel, H. A comparison of focused ion beam and electron beam induced deposition processes. *Microelectron. Reliab.* **1996**, *36*, 1779−1782.
(36) Chen, P.; van Veldhoven, E.; Sanford, C. A.; Salemink, H. W.; Maas, D. J.; Smith, D. A.; Rack, P. D.; Alkemade, P. F. Nanopillar growth by focused helium ion-beam-induced deposition. *Nanotechnology* **2010**, *21*, 455302.
(37) Thorman, R. M.; Matsuda, S. J.; McElwee-White, L.; Fairbrother, D. H. Identifying and rationalizing the differing surface reactions of low-energy electrons and ions with an organometallic precursor. *J. Phys. Chem. Lett.* **2020**, *11*, 2006−2013.
(38) Wnuk, J. D.; Gorham, J. M.; Rosenberg, S. G.; van Dorp, W. F.; Madey, T. E.; Hagen, C. W.; Fairbrother, D. H. Electron induced surface reactions of the organometallic precursor trimethyl (methylcyclopentadienyl) platinum (IV). *J. Phys. Chem. C* **2009**, *113*, 2487−2496.
(39) Wnuk, J.; Rosenberg, S.; Gorham, J.; Van Dorp, W.; Hagen, C.; Fairbrother, D. Electron beam deposition for nanofabrication: Insights from surface science. *Surf. Sci.* **2011**, *605*, 257−266.
(40) Rosenberg, S. G.; Landheer, K.; Hagen, C. W.; Fairbrother, D. H. Substrate temperature and electron fluence effects on metallic films created by electron beam induced deposition. *J. Vac. Sci. Technol., B: Nanotechnol. Microelectron.: Mater., Process., Meas., Phenom.* **2012**, *30*, 051805.
(41) Moulder, J.; Chastain, J.; King, R. *Handbook of X-ray Photoelectron Spectroscopy: A Reference Book of Standard Spectra for Identification and Interpretation of XPS Data.* ; PerkinElmer Corp., Physical Electronics Division: 1992.
(42) Wnuk, J. D.; Gorham, J. M.; Rosenberg, S. G.; van Dorp, W. F.; Madey, T. E.; Hagen, C. W.; Fairbrother, D. H. Electron beam irradiation of dimethyl-(acetylacetonate) gold (III) adsorbed onto solid substrates. *J. Appl. Phys.* **2010**, *107*, 054301.

https://doi.org/10.1021/acs.jpcc.1c05826
J. Phys. Chem. C 2021, 125, 17749−17760

(43) Plummer, E.; Salaneck, W.; Miller, J. Photoelectron spectra of transition-metal carbonyl complexes: comparison with the spectra of adsorbed CO. *Phys. Rev. B: Condens. Matter Mater. Phys.* **1978**, *18*, 1673.
(44) Zaera, F. A thermal desorption and x-ray photoelectron spectroscopy study of the surface chemistry of iron pentacarbonyl. *J. Vac. Sci. Technol., A* **1989**, *7*, 640−645.
(45) Moon, D.; Dwyer, D.; Bernasek, S. Adsorption of CO on the clean and sulfur modified Fe (100) surface. *Surf. Sci.* **1985**, *163*, 215−229.
(46) Zaera, F. A kinetic study of the chemical vapor deposition of iron films using iron pentacarbonyl. *Langmuir* **1991**, *7*, 1188−1191.
(47) Mansour, A.; Brizzolara, R. A. Characterization of the surface of FeO powder by XPS. *Surf. Sci. Spectra* **1996**, *4*, 345−350.
(48) Fujii, T.; De Groot, F.; Sawatzky, G.; Voogt, F.; Hibma, T.; Okada, K. In situ XPS analysis of various iron oxide films grown by NO_2-assisted molecular-beam epitaxy. *Phys. Rev. B: Condens. Matter Mater. Phys.* **1999**, *59*, 3195.
(49) Van Dorp, W.; Wnuk, J.; Gorham, J.; Fairbrother, D.; Madey, T.; Hagen, C. Electron induced dissociation of trimethyl (methylcyclopentadienyl) platinum (IV): Total cross section as a function of incident electron energy. *J. Appl. Phys.* **2009**, *106*, 074903.
(50) Biesinger, M. C.; Payne, B. P.; Grosvenor, A. P.; Lau, L. W.; Gerson, A. R.; Smart, R. S. C. Resolving surface chemical states in XPS analysis of first row transition metals, oxides and hydroxides: Cr, Mn, Fe, Co and Ni. *Appl. Surf. Sci.* **2011**, *257*, 2717−2730.
(51) Park, E.; Ostrovski, O.; Zhang, J.; Thomson, S.; Howe, R. Characterization of phases formed in the iron carbide process by X-ray diffraction, Mossbauer, X-ray photoelectron spectroscopy, and Raman spectroscopy analyses. *Metall. Mater. Trans. B* **2001**, *32*, 839−845.
(52) Conard, B.; Sridhar, R. Appearance potentials of ion fragments of iron pentacarbonyl. *Can. J. Chem.* **1978**, *56*, 2607−2608.
(53) Bilgilisoy, E.; Thorman, R. M.; Yu, J.-C.; Dunn, T. B.; Marbach, H.; McElwee-White, L.; Fairbrother, D. H. Surface reactions of low-energy argon ions with organometallic precursors. *J. Phys. Chem. C* **2020**, *124*, 24795−24808.
(54) Graham, R.; Bain, C.; Biebuyck, H.; Laibinis, P.; Whitesides, G. Damage of CF_3CONH-terminated organic self-assembled monolayers (SAMs) on Al, Ti, Cu, and Au by Al Kα X-rays is due principally to electrons. *J. Phys. Chem.* **1993**, *97*, 9456−9464.
(55) Belianinov, A.; Burch, M. J.; Ievlev, A.; Kim, S.; Stanford, M. G.; Mahady, K.; Lewis, B. B.; Fowlkes, J. D.; Rack, P. D.; Ovchinnikova, O. S. Direct write of 3D nanoscale mesh objects with platinum precursor via focused helium ion beam induced deposition. *Micromachines* **2020**, *11*, 527.
(56) He, S.; Tian, R.; Wu, W.; Li, W.-D.; Wang, D. Helium-ion-beam nanofabrication: extreme processes and applications. *Int. J. Extreme Manuf.* **2021**, *3*, 012001.
(57) Orús, P.; Córdoba, R.; Hlawacek, G.; De Teresa, J. M. Superconducting properties of in-plane WC nanowires grown by He^+ focused ion beam induced deposition. *Nanotechnology* **2021**, *32*, 085301.
(58) Allen, F. I. Branched high aspect ratio nanostructures fabricated by focused helium ion beam induced deposition of an insulator. *Micromachines* **2021**, *12*, 232.
(59) Córdoba, R.; Ibarra, A.; Mailly, D.; De Teresa, J. M. Vertical growth of superconducting crystalline hollow nanowires by He^+ focused ion beam induced deposition. *Nano Lett.* **2018**, *18*, 1379−1386.

https://doi.org/10.1021/acs.jpcc.1c05826
J. Phys. Chem. C 2021, 125, 17749−17760